Water Impalement Resistance and Drag Reduction of the Superhydrophobic Surface with Hydrophilic Strips

Yanlin Cao, Xiaochao Liu, Liangpei Zhang, Yanchen Wu, Chenxi You, Hongyuan Li, Huiling Duan, Jianyong Huang, and Pengyu Lv*

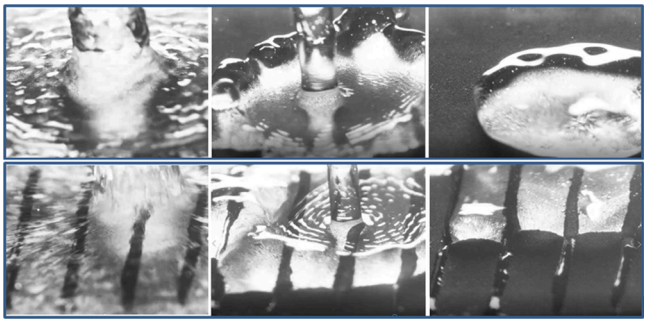

ABSTRACT: Superhydrophobic surfaces (SHS) offer versatile applications by trapping an air layer within microstructures, while water jet impact can destabilize this air layer and deactivate the functions of the SHS. The current work presents for the first time that introducing parallel hydrophilic strips to SHS (SHS-s) can simultaneously improve both water impalement resistance and drag reduction (DR). Compared with SHS, SHS-s demonstrates a 125% increase in the enduring time against the impact of water jet with velocity of 11.9 m/s and a 97% improvement in DR at a Reynolds number of 1.4×10^4. The key mechanism lies in the enhanced stability of the air layer due to air confinement by the adjacent three-phase contact lines. These lines not only impede air drainage through the surface microstructures during water jet impact, entrapping the air layer to resist water impalement, but also prevent air floating up due to buoyancy in Taylor−Couette flow, ensuring an even spread of the air layer all over the rotor, boosting DR. Moreover, failure modes of SHS under water jet impact are revealed to be related to air layer decay and surface structure destruction. This mass-producible structured surface holds the potential for widespread use in DR for hulls, autonomous underwater vehicles, and submarines.

KEYWORDS: *superhydrophobic surface, parallel hydrophilic strips, water impalement resistance, drag reduction, air confinement*

1 . INTRODUCTION

Inspired by lotus leaf, legs of water strider, rice leaf, springtail, and other aquatic creatures,[1] superhydrophobic surfaces (SHSs) have been widely investigated due to their great potential applications in the fields of anti-icing,[2,3] anticorrosion,[4−6] antifouling,[5,7] self-cleaning,[8] and drag reduction (DR),[9−12] because of the existence of an air layer entrapped in the microstructures to form the Cassie state. In general, the performance of SHSs refers to the wettability characterized by the water contact angle (CA) and rolling angle (RA), while the ability to resist water impalement is another key performance. When a ship or underwater vehicle travels through water, it is inevitably subjected to the impact of water flow with high velocity, which tends to cause the Cassie−Wenzel transition on SHS[13,14] and thus weakens or even loses the functions of SHS.[9,15,16]

The water impalement resistance of SHS depends on the capillary pressure (P_c), dynamic impact pressure (P_d), and water hammer pressure (P_{wh}).[17,18] When $P_c > P_{wh} > P_d$, SHS will not be impaled. To enhance the water impalement resistance of SHS, efforts have been done to increase P_c by adjusting the pore dimension of SHS[19−21] or reducing the surface energy,[17] decrease P_{wh} by using a flexible binder,[17,21,22] and conduct a combination of both.[17,21] Zhang et al.[20] used a two-step spraying technique to prepare an impact-resistant SHS that can withstand the impact of a water jet with velocity of 9.5 m/s for 60 s without damage. The two-step spraying technique minimizes the pore radius of the capillaries of SHS. Luo et al.[21] fabricated impact-resistant superhydrophobic coatings using a flexible binder and a two-step spraying technique. At an impact speed of 11.4 m/s, the surface can remain superhydrophobic for 114 s. To further enhance the impalement resistance, Peng et al.[17] employed fluoride reagents including perfluoropolyether, polytetrafluoroethylene, and fluorinated modified epoxy resin to develop all-organic superhydrophobic coatings. The incorporation of both flexible and low surface energy materials enabled the coating to maintain the Cassie state even after 200 s of water impact at 25 m/s. However, the use of fluorinated materials should be avoided during the preparation of SHS considering the safety and environmental protection.[23]

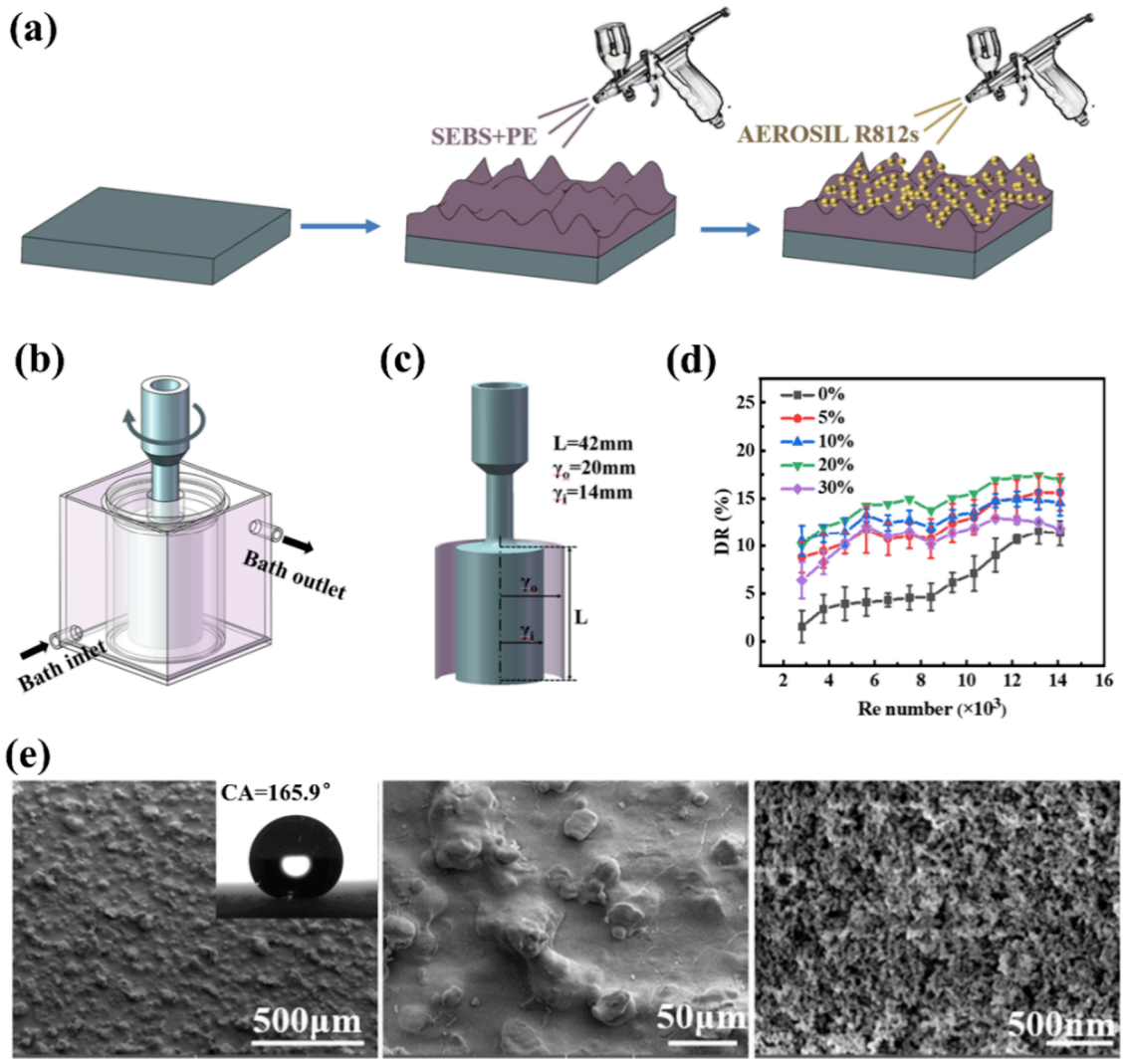

Figure 1. (a) Schematic diagram of the preparation process of SHS. (b) Schematic of the TC device with a water bath circulation system. (c) Schematic of the TC inner rotor with a dimension scale. (d) DR of superhydrophobic coatings with different PE contents at different Reynolds numbers. (e) SEM images and CA of the superhydrophobic surface with 20% PE content at different magnifications.

The water impalement resistance of SHS can also be improved by preparing special microstructures[24−28] or tuning the flexibility of substrate.[29] Yun et al.[25] prepared super-omniphobic surfaces with microscale wrinkles and serif-T-shaped nanostructures that were resistant to the impalement of water droplets and even ethanol droplets, while the processes such as electron beam sputtering and lithography hinder the large-scale preparation of this surface. Vasileiou et al.[29] enhanced the water repellency of substrate by tuning its flexibility, which however limited the application of this method on rigid substrates.

It is well known that SHS can reduce flow frictional resistance and thus decrease fuel consumption of the hull.[10,30,31] However, the air layer on SHS is susceptible to disruption from water impact,[13] resulting in wetting and reduction of DR.[9] Thus, excellent ability of SHS to resist water impalement ensures a sustainable and stable DR.[14] To the best of our knowledge, few articles have investigated both water impalement resistance and DR concurrently.

In this paper, we propose a new method of introducing parallel hydrophilic strips to the random-roughness SHS that can simultaneously improve both water impalement resistance and DR. These impalement-resistant drag-reducing surfaces (SHS-s) are cost-effective, are free of fluorine, and can be easily manufactured on a large scale. SHSs were able to withstand the impact of water jets at speeds of 11.9 8.9, 6, and 4 m/s for 160, 1140, 2100, and 144,000 s, respectively. The DR of SHS was measured to be 16.9% at a Reynolds number of 1.4×10^4. Compared with SHS, the durations of SHS-s against the impact of water jet increased to 360, 2100, 3600, and 252,000 s at the same water jet speeds, and the DR at the same Reynolds number elevated to 33.3%. The mechanisms for enhancing water impalement resistance and DR were clarified experimentally. Furthermore, different failure modes of SHS under water jet impacts with short and long durations were discovered to be the decay of the air layer and the destruction of surface structures, respectively.

2. RESULTS AND DISCUSSION

2.1. Performance Characterization of SHS. The SHSs were prepared using a two-step spraying technique (Figure 1a). DR of SHS was tested using a Taylor−Couette (TC) device that consists of an inner rotor and an outer rotor (refer to Figure 1b). The specific dimensions of the inner rotor can be

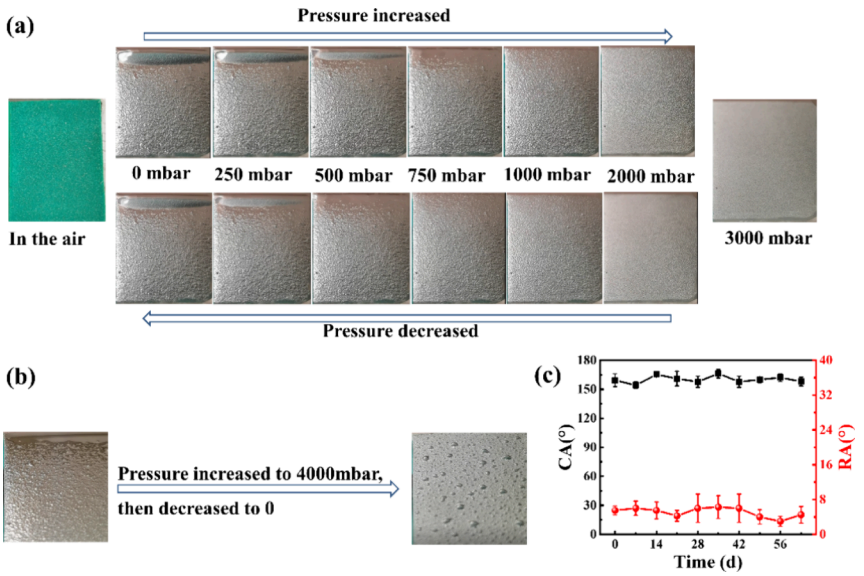

Figure 2. Hydrostatic pressure resistance of SHS at (a) 0−3000 mbar (the superhydrophobic surface appeared green in air, but when submerged, it took on a silvery hue due to the presence of an air layer), and (b) 0−4000 mbar. (c) CA and RA of the SHS as a function of immersion time in seawater.

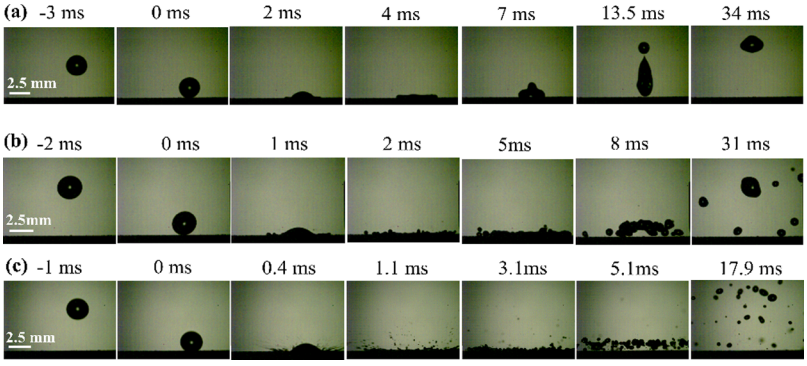

Figure 3. A water droplet impacted SHS at (a) 1, (b) 2, and (c) 5 m/s, respectively, with no signs of impalement.

seen in Figure 1c. The SHS with different mass fractions of polyethylene (PE) microparticles exhibited different DR within the range of Reynolds numbers from 2.8×10^3 to 14×10^3, as shown in Figure 1d. The highest DR was achieved when the mass fraction of the PE microparticles was 20%. This formulation was used for all of the subsequent studies. The SEM images showed that the SHS possessed hierarchical structures consisting of microprotrusions and nanoparticles (Figure 1e). As demonstrated in Figure S1, the SHS maintained a CA above 150° and an RA below 10° after 12 cycles of tape peeling or exposure to 200 g of sand impact, indicating its superior mechanical durability.

Maintaining the air layer on the SHS is crucial for practical applications.[32,33] To examine the air layer stability of SHS, hydrostatic pressure was first applied to the submerged sample (Figure 2a,b). At low hydrostatic pressure (0−3000 mbar), the air on the surface was compressed into the micronano structure's pores as pressure increased, and the surface retained a silvery reflection due to the stable presence of air. Upon release of the pressure, the air layer of the SHS recovered, indicating the stability of the air layer. However, when a higher hydrostatic pressure of 4000 mbar was applied, only single independent bubbles were formed on the SHS after reducing the pressure, in which the air layer was not able to recover as before. Second, SHS was immersed in seawater. It should be noted that we define an SHS as one surface with a CA > 150° and an RA < 10°. If the RA exceeds 10° or the CA falls below 150°, the SHS loses its superhydrophobicity. After 8 weeks of immersion, the superhydrophobicity of SHS was still retained, indicating its potential for long-term DR (Figure 2c).

The impalement resistance of the SHS to water droplet was thoroughly investigated (Movie S1, Movie S2, and Movie S3). Important moments during the droplet impact experiments at various velocities were captured (Figure 3). At a low velocity of 1 m/s, the droplet impacted the surface and rebounded. At a higher speed of 5 m/s, the droplet splashed into numerous tiny droplets that were highly mobile on the surface. The contact time was 5.1 ms for 5 m/s as opposed to 13.5 ms for 1 m/s, which could be attributed to splashing at a higher Weber number ($We = \rho v^2 D/\gamma$, where ρ, v, D, and γ represent the density, velocity, diameter of water droplets or water jets, and surface tension of water, respectively).[34] No puncture marks, such as tiny droplet residue[35] or liquid patches,[36] were observed after droplet impact, implying excellent superhydrophobicity of the SHS.

2.2. Performance Characterization of the SHS-h and SHS-s-8 mm. Certain biological surfaces in nature have hydrophilic and hydrophobic regions coexisting to achieve

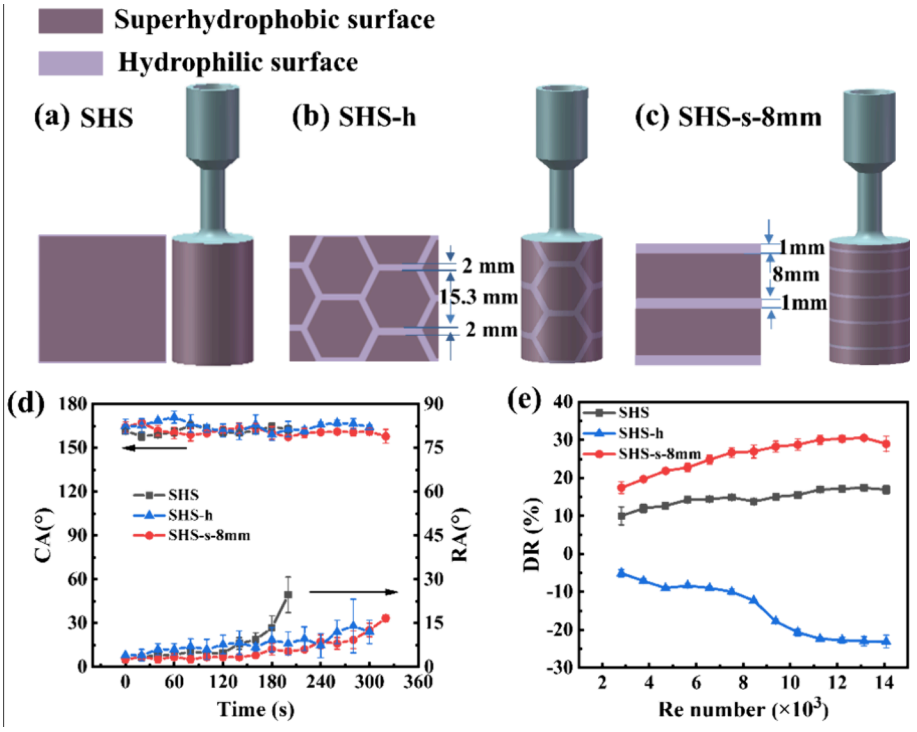

Figure 4. (a) Schematic diagram of SHS on a flat aluminum plate (left) and a TC rotor (right). (b) Schematic diagram of SHS-h on a flat aluminum plate (left) and a TC rotor (right). (c) Schematic diagram of SHS-s-8 mm on a flat aluminum plate (left) and a TC rotor (right). (d) Variation of CA and RA with the water impact time on three different surfaces. Note that the CA and RA of SHS-h or SHS-s refer to CA and SA in the superhydrophobic region. (e) DR for three different surfaces at different Reynolds numbers.

specific functions. For instance, the back of the desert beetle has both hydrophobic and hexagonal-like hydrophilic regions.[37] Taking inspiration from this, we added hydrophilic orthohexagonal patterns or parallel hydrophilic strips to the SHS to investigate whether they could improve water impalement resistance and DR (Figure 4a–c). To create a surface with hydrophilic patterns, a marker pen was employed to draw the hydrophilic design on the SHS using a PPS mask obtained through laser cutting, as illustrated in Figure S2. Wherever the marker pen passes through the PPS mask, the superhydrophobic area transforms into hydrophilic. The CA of the hydrophilic region is 79.5°, as shown in Figure S3a. The different surfaces are shown in Figure S3b–d. The geometric parameters of the SHS-h and SHS-s-8 mm are depicted in Figure 4b, c. The SHS-h and SHS-s-8 mm were able to maintain their Cassie states for up to 240 and 280 s when subjected to a water jet with an impact velocity of 11.9 m/s in the normal direction (Figure 4d), representing 50 and 75% increases in duration compared with that of SHS, respectively. However, the addition of hydrophilic ortho-hexagons to the SHS resulted in increased drag, whereas SHS-s-8 mm exhibited improved DR, as demonstrated in Figure 4e.

2.3. Performance Optimization by Using SHS-s. To investigate the effect of hydrophilic strip spacing on DR, we prepared SHS with varying hydrophilic strip spacings (Figure S4) and tested their DR (Figure 5a). Our experimental results indicate that incorporating parallel hydrophilic strips into SHS improved their DR. Specifically, the DR of SHS-s-6 mm was improved by 64 to 97% within the Reynolds number range of 2.8×10^3–1.4×10^4 compared with that of pure SHS (Figure 5a). When the TC rotor with SHS was submerged in water, the air layer on the SHS accumulated at the top of the rotor due to buoyancy (Figure 5b). This led to the exposure of the roughness at the bottom of the rotor and an increase in form resistance.[38,39] When the TC rotor with SHS-s-6 mm was submerged in water, the air layer is uniformly distributed on the SHS between the hydrophilic strips (Figure 5b) due to the energy barriers caused by the hydrophilic strips.[40] It is the stabilized air layer pinned by hydrophilic strips that results in improved DR. Similar results have been reported in other literature.[40,41]

However, different from the previous work of Hu et al.,[40] in the current work, no additional air is injected to change the air ring shapes before the DR tests. This is because the emphasis of our study lies in exploiting the impalement-resistance potential of partially superhydrophobic and hydrophilic surfaces under the premise of acceptable DR. As expected, the rotor surface, featuring alternating superhydrophobic strips and hydrophilic strips, but without abundant air injection, exhibits considerable DR across a wider range of Reynolds numbers (2.8×10^3–1.4×10^4). Despite the fact that the peak DR in our work is lower than that reported at the same *Re* in Hu et al.'s study,[40] it is reasonable and perceived as the trade-off between considerable DR and excellent water impalement resistance.

The SHS-s-4 mm, SHS-s-6 mm, and SHS-s-8 mm surfaces exhibited significantly improved DR, prompting further investigation of their water impalement resistance. Water jets with speeds (corresponding *We*) of 11.9 m/s (13616.3), 8.9 m/s (9792.4), 6 m/s (3461.5), and 4 m/s (1538.5) were generated using water pumps. Experimental results revealed that the SHS-s-4 mm, SHS-s-6 mm, and SHS-s-8 mm surfaces displayed similar water impalement resistance under a water jet flow of 11.9 m/s (Figure 5c). Among different surfaces, the SHS-s-6 mm demonstrated optimal DR and water impalement

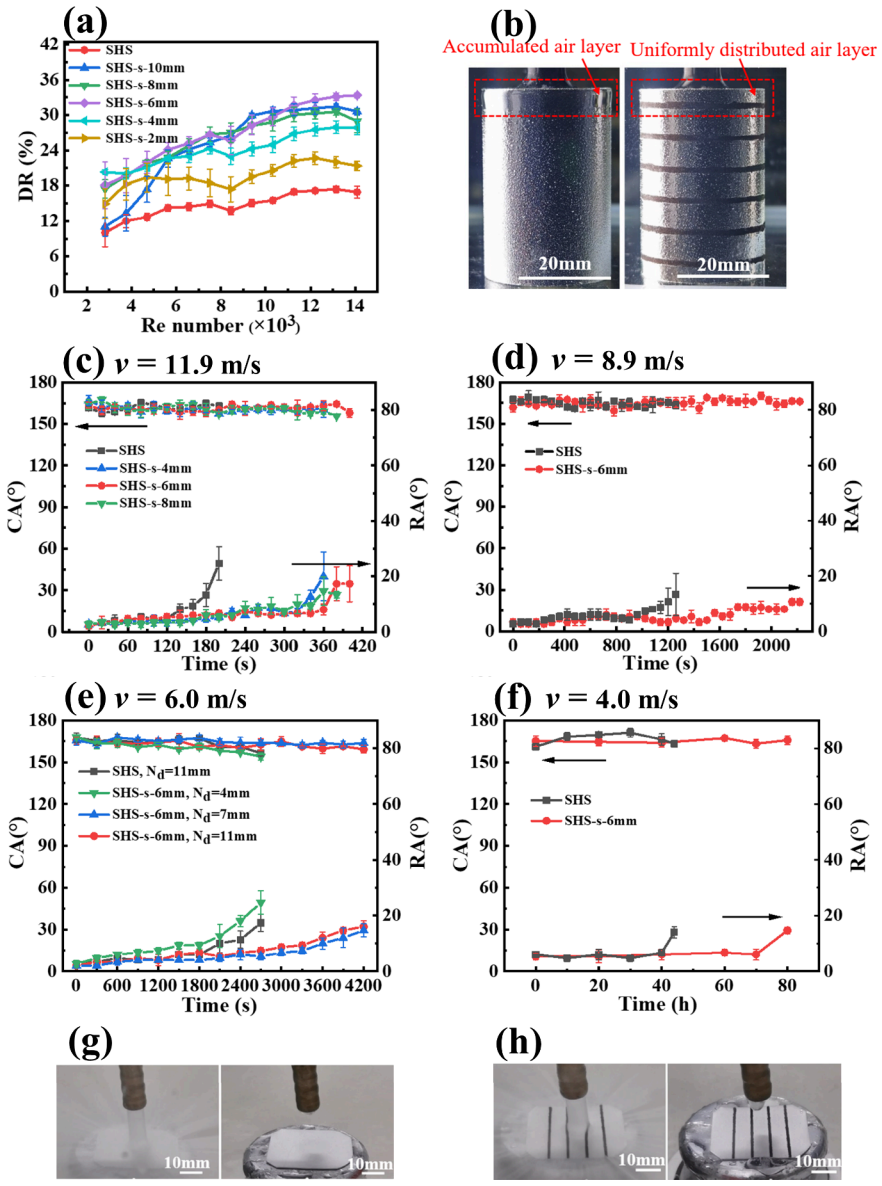

Figure 5. DR and water impalement resistance of the SHS and SHS-s surfaces. (a) DR for surfaces with different superhydrophobic strips at different Reynolds numbers. (b) Left: the air layer on the TC inner rotor with the SHS surface (inside the rectangular box is the accumulated air layer due to buoyancy); right: the air layer on the TC inner rotor with an SHS-s-6 mm surface (inside the rectangular box is the uniformly distributed air layer due to hydrophilic strips). Variations in water CA and RA on different surfaces as a function of impacting time of water jet at velocities of (c) 11.9 m/s, (d) 8.9 m/s, (e) 6 m/s (N_d = 4, 7, and 11 mm), and (f) 4 m/s. Captured images of the water jet impacting on (g) SHS and (h) SHS-s-6 mm at a speed of 11.9 m/s.

resistance, and thus, it was chosen for the subsequent water impact test.

When subjected to water jets in the normal direction at velocities of 11.9, 8.9, 6, and 4 m/s, the SHS-s-6 mm maintained the Cassie−Baxter state for 360, 2100, 3600, and 252,000 s, respectively. In contrast, the SHS remained in the Cassie−Baxter state for 160, 1140, 2100, and 144,000 s, respectively (Figure 5c−f). Additionally, experiments have been conducted on the SHS-s-6 mm by using three nozzles with different nozzle diameters N_d (4, 7, and 11 mm). As shown in Figure 5e, when the nozzle size exceeds the interval width between stripes, specifically N_d = 7, 11 mm > 6 mm, the jet impact area covers both SHS and hydrophilic stripes, leading to significant and consistent impalement resistance effects. On the contrary, for the case of N_d = 4 mm < 6 mm, where water jet impacts on the area of pure SHS without touching the hydrophilic stripes, the duration of the SHS-s-6 mm against the jet impact is similar to that of the SHS, exhibiting no impalement resistance effects. This influence of nozzle sizes on durations can further highlight the importance of the hydrophilic stripes in water impalement resistance.

No water droplets were left on both the SHS and SHS-s-6 mm surfaces until they were respectively impacted by water jets with a velocity of 11.9 m/s for durations exceeding 160 and 360 s (Figure 5g,h and Movies S4 and S5).

The water jet impact resistance of SHS and SHS-s-6 mm at varying velocities is summarized in Figure 6a. The results show that the addition of parallel hydrophilic strips enhances the impalement resistance of SHS-s-6 mm against water jets. During impact, a water film formed on the surface. The water

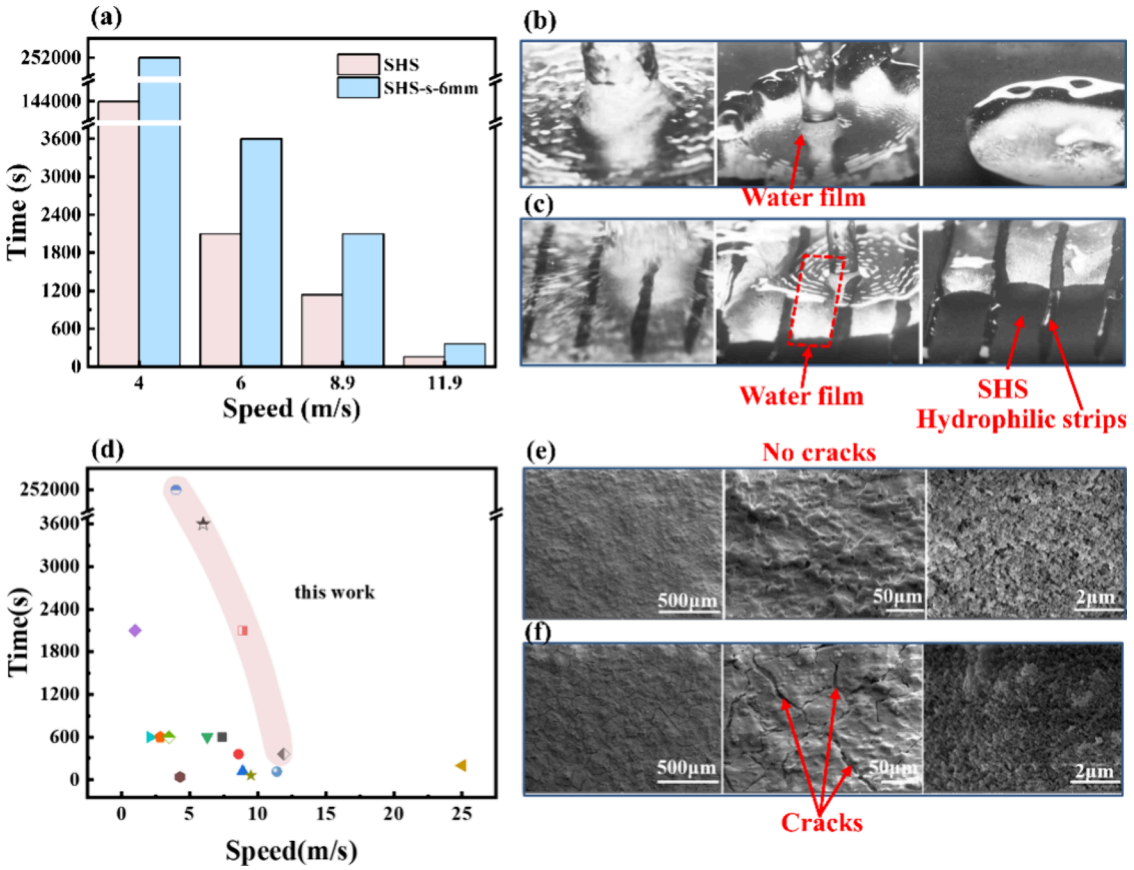

Figure 6. (a) Enduring time of different surfaces against the impact of water jets with different velocities. (b) The water film on the SHS after water jet impact ends. (c) The water film on the SHS-s-6 mm after water jet impact ends (inside the prism frame is a relatively closed environment formed by a water film, hydrophilic strips, and the bottom superhydrophobic surface). (d) Comparison of water jet impact resistances of different SHSs corresponding to Table S1. Data from literature and the current work. SEM images of (e) SHS-s-6 mm after being impacted for 380 s at a speed of 11.9 m/s and (f) SHS-s-6 mm after experiencing an 80 h impact at a speed of 4 m/s at different magnifications.

film could be clearly seen especially when the water jet impact ended (Figure 6b,c and Movie S6). When the water jet impacted on SHS, the air under the water film drained everywhere along the surface structures of SHS. When the water jet impacted on the SHS-s-6 mm, the water film, together with the bottom SHS and the adjacent hydrophilic strips, created a relatively enclosed environment that stabilized the air layer (Figure 6c), which could be easily observed under low velocity water jets in Movie S7.

In the following discussion, we consider a representative volume element (REV) extracted from the microstructure of SHS and assume a mechanical quasi-static equilibrium within the REV. First, microscale balance of pressure can be derived from the Laplace equation, expressed as

$$P_L - P_G = P_{Laplace} \tag{1}$$

Here, the hydro-pressure P_L is mostly induced by water hammer and the Laplacian pressure $P_{Laplace}$ is limited by capillary pressure P_c, i.e., $P_{Laplace} < P_c$. Moreover, the gas pressure P_G of REV is obtained by the equation of state for isothermal ideal gas

$$\frac{P_{G,0}V_0}{n_0} = \frac{P_{G,t}V_t}{n_t} \tag{2}$$

where the subscripts 0 and t denote the initial state and the state at t, respectively. The REV volume is presumed to remain constant before the microstructure of the SHS is disrupted by the water impact, i.e., $V_0 \cong V_t$. As a result, $P_{G,t}$ and the moles of gas n_t share a similar trend during jet impacts. As observed in experiments, the gas inside the cavities of SHS is continuously entrained by a water jet, leading to a gradual decrease in n_t and consequently a decline in $P_{G,t}$. From eq 1, decreasing $P_{G,t}$ with constant P_L (invariant jet at a single case) contribute to the rise of $P_{Laplace}$ until $P_L - P_G > P_c$ where the impalement occurs.

In our design, the hydrophilic stripes distributed on SHS serve as barriers to prevent air escape induced by a water jet, which lower the loss rate of n_t and that of $P_{G,t}$. According to the aforementioned analysis, our design can therefore delay the implementation process, which is termed as impalement resistance.

Additionally, the water film may be able to cushion the impact of the water jet. This combination of a stabilized air layer and cushioning effect of the water film results in a significantly enhanced impalement resistance of the SHS-s-6 mm surface.

Compared with other nonfluorinated SHS reported in the literature, the SHS-s-6 mm presented in this work demonstrates superior water impalement resistance, even surpassing most fluorinated SHS (refer to Figure 6d and Table S1 for details). The superior water impalement resistance can be attributed to several factors, including the pores between nanoparticles on the SHS, the flexibility of the SEBS binder, the strong bonding between nanoparticles and the binder, the stable air layer, and the possible buffering by the water film.

The two-step spraying technique ensures that the pores between nanoparticles on the SHS are sufficiently small to generate a capillary pressure large enough to resist water impalement. The flexible SEBS binder aids in dissipating the impact energy, and the strong bonding between the nanoparticles and SEBS enables them to remain firmly in place, even after 80 h of impact (as shown in Figure 6f). Although there are many SHSs with various hydrophilic patterns, we only studied two typical surfaces, namely, SHS-h and SHS-s, because SHS-s-6 mm already exhibits enhanced impalement resistance and improved DR compared with the pure SHS.

After 380 s of water jet impact of 11.9 m/s, the CA of SHS-s-6 mm was 160.2 ± 1.2° while the RA was over 10°. Unexpectedly, after drying, the CA increased to 163 ± 3.2° and the RA decreased to 8.6 ± 1.2° (as shown in Table S2). SEM revealed that the micro- and nanostructures on the SHS remained intact (Figure 6e), which differed from previous reports in the literature where the structure of the SHS was destroyed, resulting in a loss of superhydrophobicity.[21,22] The structural integrity indicates that the failure of the SHS is solely due to the replacement of air within the micronano structure by water, and once dried, the superhydrophobic properties are restored.

After being exposed to a 4 m/s jet for 80 h, the RA of SHS-s-6 mm exceeded 10° and it still remained over 10° even after the surface dried (as presented in Table S2). A considerable amount of cracks formed on the surface after prolonged impact; however, the nanostructure remained unharmed, as observed in the SEM images (Figure 6f), which also explains why CA remained almost unchanged. These cracks increased the RA of the SHS, which in turn led to the failure of the SHS, and the superhydrophobicity cannot be recovered by drying.

In general, for the case of short duration of water jet impact even under high speed (11.9 m/s), the loss of surface superhydrophobicity is attributed to the replacement of air inside the micronano structure by water and the superhydrophobicity can be recovered by drying. For the case of long-time impact even under low-speed water jet impact (4 m/s), the loss of surface superhydrophobicity is due to the material fatigue of the surface structure and it cannot be recovered by drying.

3. CONCLUSIONS

This study is the first to demonstrate that the introduction of parallel hydrophilic strips to a random-roughness SHS can simultaneously enhance water impalement resistance and DR. After the incorporation of hydrophilic strips, the SHS-s-6 mm surface could withstand water jet impact at velocities of 11.9, 8.9, 6, and 4 m/s for durations of up to 360, 2100, 3600, and 252,000 s, respectively. This represents improvements of nearly 125, 84, 71, and 75% compared with the original SHS. The impalement resistance of the fluorine-free SHS-s-6 mm surfaces exceeds that of most SHS reported in the literature, even those containing fluorine. Compared with SHS, the DR of SHS-s-6 mm increased by 97% at a Reynolds number of 1.4×10^4, reaching a maximum DR of 33.3%. The enhanced stability of the air layer increases the water impalement resistance, while the uniform distribution of air layer leads to improved DR. Additionally, after a short-time impact of a water jet under high impact speed, the lost superhydrophobicity could be recovered by drying. The structure of the SHS remained intact but the air within the nanostructure was replaced by water, resulting in the loss of superhydrophobicity. However, after a long-time impact, numerous cracks appear, resulting in an increase in RA, and its superhydrophobic properties could not be restored by drying. This low-cost, mass-producible, fluorine-free, impalement-resistant, and drag-reducing surface holds great promise for the DR of hulls, autonomous underwater vehicles, and submarines.

4. EXPERIMENTAL SECTION

4.1. Materials. Styrene ethylenebutylenestyrene copolymer (SEBS) was purchased from Boruida New Material Co. Polyethylene micrometer particles (PE, 2000 mesh) were purchased from Zhonglian Plastic Chemical Co. Butyl acetate and ethyl acetate were supplied by the Beijing Tongguang Fine Chemical Co. Hydrophobic fumed silica (AEROSIL R812s) was purchased from Evonik. Polyphenylene sulfide (PPS) plastic sheet was provided by Jinzhuo Plastic Industry Co. The marker pens (EB-150) used to draw hydrophilic patterns were purchased from Kokuyo Commercial Shanghai Co. The seawater was taken from the seashore of Weihai City, Shandong Province, China. All reagents were used as received.

4.2. Preparation and Characterization of Superhydrophobic Surfaces and Superhydrophobic Surfaces with Hydrophilic Patterns. To obtain the binder dispersion, SEBS (6 g) was dissolved in butyl acetate (94 g), and the corresponding mass (0 0 3, 0 6, 1.2, 1.8 g) of PE was added to produce micrometer roughness and thoroughly mixed. AEROSIL R812s (3.6 g) was ultrasonically dispersed in a solvent mixture of ethyl acetate and butyl acetate (180 mL). The substrate was first sprayed with the binder dispersion, followed by repeating the spraying process four times. The AEROSIL R812s dispersion was then sprayed onto the SEBS layer, and the process was repeated four times. After drying, AEROSIL R812s nanoparticles were firmly attached to the binder, leading to an SHS. The microstructure of the SHS was observed by scanning electron microscopy (MAIA3 model 2016, TESCAN, Czech).

To incorporate hydrophilic strips into the SHS, masks featuring parallel strips were cut from a PPS plastic sheet using a laser cutting machine. The strips had a width of 1 mm and intervals of i mm (i = 2, 4, 6, 8, or 10). Employing these masks, parallel hydrophilic strips were drawn onto the SHS with a marker pen. The resulting SHS-s were denoted as SHS-s-i mm (i = 2, 4, 6, 8, or 10) (Figure S4). In addition, the SHS with hydrophilic hexagonal patterns, denoted as SHS-h, was obtained by using the same method as described above.

4.3. Testing of Wettability. The wettability tests were conducted using a contact angle meter (OCA20, DataPhysics, Germany). The CA and RA were measured using 6 and 8 μL drops of water, respectively. Each value for CA and RA is the average of measurements taken at four different locations.

4.4. Testing of Mechanical Durability. The mechanical durability of the SHS was assessed by tape peeling and sand impact tests. Tape peeling tests were performed using 3M's VHB 4910 tape, with a new tape used for each test cycle. In each cycle, a 200 g weight was rolled over the tape twice, followed by tape peeling. The CA and RA were measured every two cycles until the CA dropped below 150° or the RA exceeded 10°. In the quartz sand (40−70 mesh) impact test, the SHS was inclined at a 45°angle and a sand container was positioned at a height of 40 cm above the SHS. To ensure that all sand impacted the same location, a tube was used to extend the lower end of sand container to the position right above the SHS.

4.5. Testing of Water Impalement Resistance. In the water droplet impact test, a transfer pipet was used to release 8 μL water droplets. These droplets fell freely from predetermined heights (5.1, 20.4, and 127.6 cm) onto the SHS and their impact was recorded by a high-speed camera (Phantom Miro C210, Phantom, USA).

In the water jet impact test, a water circulation system was used to generate water jets with different speeds (11.9, 8.9, 6, and 4 m/s). The system consisted of a circulation pump and a water tank with a flow regulator installed in the middle of the outlet pipe to adjust the water flow rate. The velocity of water jet flow was calculated using the following equation:

$$v = \frac{V}{\pi r^2 t} \tag{3}$$

where V is the volume of water flowing out at a certain time t and r is the radius of the outlet hole.

4.6. Testing of Drag Reduction. We conducted a DR experiment using a Taylor−Couette (TC) device that consists of inner and outer rotors. The inner rotor, which has a precision of approximately 20 μm, is mounted to the freely rotating spindle of a rheometer (DHR-2, TA Instruments, USA). The inner cylinder has a radius of $r_i = 14 \pm 0.02$ mm and the outer cylinder has a radius of $r_0 = 20 \pm 0.02$ mm, giving a radius ratio of $\eta = 0.7$. The height of setup is $L = 42 \pm 0.02$ mm, rendering an aspect ratio of $\Gamma = L/d = 7$ due to the fact that the gap between the two cylinders is $d = r_0 - r_i = 6$ mm. Throughout the experiments, the outer cylinder remained fixed and the overall torque of the system was measured by the torque sensor of the rheometer. Reynolds number is defined by

$$Re = \frac{r_i \omega_i d}{v} \tag{4}$$

where ω_i is the angular velocity of the inner rotor and ν is the kinematic viscosity. In the present work, ω_i ranges from 30 to 150 rad/s, corresponding to a range of Re from 2.8×10^3 to 1.4×10^4. The working liquid is ultrapure water at a temperature of 25 °C, with a density of $\rho = 997$ kg·m^{-3} and kinematic viscosity of $v = 0.897 \times 10^{-6}$ m^2·s^{-1}. The outer cylinder was surrounded by a PMMA cubic circulating bath, which maintained a constant temperature for the system.

The total measured torque (T_s) consists of two components, T and T_b, corresponding to the frictional resistances caused by the sides and the top/bottom ends of the cylinder, respectively. To determine T_b, we used the linearization method previously employed by Greidanus et al.[42] Therefore, T is calculated by subtracting the measured T_b from the measured T_s, as detailed in the previous article.[43] For each speed, the torque T_s is measured for 30 s and three tests are conducted, with the torque averaged across all runs. DR is defined as

$$\mathrm{DR} = \frac{T_{ss} - T_{sc}}{T_{ss} - T_b} \times 100\% \tag{5}$$

where T_{ss} and T_{sc} represent the total torque of the smooth uncoated and coated inner rotors, respectively.

AUTHOR INFORMATION

Corresponding Author

Pengyu Lv − *State Key Laboratory for Turbulence and Complex Systems, Department of Mechanics and Engineering Science, BIC-ESAT, College of Engineering, Peking University, Beijing 100871, China; Laoshan Laboratory, Qingdao 266237, People's Republic of China;* orcid.org/0009-0006-6943-7245; Email: lvpy@pku.edu.cn

Authors

Yanlin Cao − *State Key Laboratory for Turbulence and Complex Systems, Department of Mechanics and Engineering Science, BIC-ESAT, College of Engineering, Peking University, Beijing 100871, China; Laoshan Laboratory, Qingdao 266237, People's Republic of China*

Xiaochao Liu − *State Key Laboratory for Turbulence and Complex Systems, Department of Mechanics and Engineering Science, BIC-ESAT, College of Engineering, Peking University, Beijing 100871, China; Laoshan Laboratory, Qingdao 266237, People's Republic of China*

Liangpei Zhang − *State Key Laboratory for Turbulence and Complex Systems, Department of Mechanics and Engineering Science, BIC-ESAT, College of Engineering, Peking University, Beijing 100871, China*

Yanchen Wu − *Institute for Applied Materials-Microstructure Modeling and Simulation, Karlsruhe Institute of Technology, Karlsruhe 76131, Germany; Institute of Nanotechnology, Karlsruhe Institute of Technology, Eggenstein-Leopoldshafen 76344, Germany*

Chenxi You − *State Key Laboratory for Turbulence and Complex Systems, Department of Mechanics and Engineering Science, BIC-ESAT, College of Engineering, Peking University, Beijing 100871, China*

Hongyuan Li − *State Key Laboratory for Turbulence and Complex Systems, Department of Mechanics and Engineering Science, BIC-ESAT, College of Engineering, Peking University, Beijing 100871, China; Laoshan Laboratory, Qingdao 266237, People's Republic of China*

Huiling Duan − *State Key Laboratory for Turbulence and Complex Systems, Department of Mechanics and Engineering Science, BIC-ESAT, College of Engineering, Peking University, Beijing 100871, China*

Jianyong Huang − *State Key Laboratory for Turbulence and Complex Systems, Department of Mechanics and Engineering Science, BIC-ESAT, College of Engineering, Peking University, Beijing 100871, China;* orcid.org/0000-0002-6581-895X

Author Contributions

Y.C. conceived the idea, designed the experiments, carried out the experiments, and wrote the manuscript. X.L. assisted in conducting the drag reduction tests. L.Z. assisted in conducting water impact experiments. Y.W. and C.Y. assisted in data analysis. H.L. helped validate the experiments. P.L., H.D., and J.H. supervised the research and revised the manuscript.

Notes

The authors declare no competing financial interest.

ACKNOWLEDGMENTS

This work was supported financially by the National Natural Science foundation of China (NSFC) (Nos. 12293000, 12293001, 11988102, 12172006, U2141251) and Laoshan Laboratory (No. LSKJ202200500).

REFERENCES

(1) Choi, J.; Jo, W.; Lee, S. Y.; Jung, Y. S.; Kim, S.-H.; Kim, H.-T. Flexible and robust superomniphobic surfaces created by localized photofluidization of azopolymer pillars. *ACS Nano* **2017**, *11*, 7821−7828.

(2) Wang, L.; Gong, Q.; Zhan, S.; Jiang, L.; Zheng, Y. Robust Anti-Icing Performance of a Flexible Superhydrophobic Surface. *Adv. Mater.* **2016**, *28*, 7729−7735.

(3) Zhang, C.; Xie, H.; Du, Y.; Li, X.; Zhou, W.; Wu, T.; Qu, J. Shelter Forest Inspired Superhydrophobic Flame-Retardant Composite with Root-Soil Interlocked Micro/Nanostructure Enhanced Mechanical. *Phys. Chem. Durability Adv. Funct Mater.* **2023**, *33*, No. 2213398.

(4) Zhang, H.; Bu, X.; Li, W.; Cui, M.; Ji, X.; Tao, F.; Gai, L.; Jiang, H.; Liu, L.; Wang, Z. A skin-inspired design integrating mechano−chemical−thermal robustness into Superhydrophobic coatings. *Adv. Mater.* **2022**, *34*, 8.

(5) Liu, Z.; Zhang, C.; Jing, J.; Zhang, X.; Wang, C.; Liu, F.; Jiang, M.; Wang, H. Bristle worm inspired ultra-durable Superhydrophobic coating with repairable microstructures and anti-corrosion/scaling properties. *Chem. Eng. J.* **2022**, *436*, 10.

(6) Sow, P. K.; Singhal, R.; Sahoo, P.; Radhakanth, S. Fabricating low-cost, robust Superhydrophobic coatings with re-entrant topology for self-cleaning, corrosion inhibition, and oil-water separation. *J. Colloid Interface Sci.* **2021**, *600*, 358−372.

(7) Yin, Z.; Yuan, F.; Xue, M.; Xue, Y.; Xie, Y.; Ou, J.; Luo, Y.; Hong, Z.; Xie, C. A multifunctional and environmentally safe Superhydrophobic membrane with superior oil/water separation, photocatalytic degradation and anti-biofouling performance. *J. Colloid Interface Sci.* **2022**, *611*, 93−104.

(8) Geyer, F.; D'Acunzi, M.; Sharifi-Aghili, A.; Saal, A.; Gao, N.; Kaltbeitzel, A.; Sloot, T. F.; Berger, R.; Butt, H. J.; Vollmer, D. When and how self-cleaning of Superhydrophobic surfaces works. *Sci. Adv.* **2020**, *6*, No. eaaw9727.

(9) Xu, M.; Yu, N.; Kim, J.; Kim, C. J. ". Superhydrophobic drag reduction in high-speed towing tank. *J. Fluid Mech.* **2021**, *908*, A6.

(10) Feng, X.; Sun, P.; Tian, G. Recent developments of Superhydrophobic surfaces (SHS) for underwater drag reduction opportunities and challenges. *Adv. Mater. Inter.* **2022**, *9*, No. 2101616.

(11) Zhang, S.; Ouyang, X.; Li, J.; Gao, S.; Han, S.; Liu, L.; Wei, H. Underwater drag-reducing effect of Superhydrophobic submarine model. *Langmuir.* **2015**, *31*, 587−593.

(12) Tricinci, O.; Pignatelli, F.; Mattoli, V. 3D Micropatterned Functional Surface Inspired by Salvinia Molesta via Direct Laser Lithography for Air Retention and Drag Reduction. *Adv. Funct Mater.* **2023**, *33*, No. 2206946.

(13) Papadopoulos, P.; Mammen, L.; Deng, X.; Vollmer, D.; Butt, H.-J. How superhydrophobicity breaks down. *Proc. Natl. Acad. Sci. U.S.A.* **2013**, *110*, 3254−3258.

(14) Li, Z.; Marlena, J.; Pranantyo, D.; Nguyen, B. L.; Yap, C. H. A porous Superhydrophobic surface with active air plastron control for drag reduction and fluid impalement resistance. *J. Mater. Chem. A* **2019**, *7*, 16387−16396.

(15) Aljallis, E.; Sarshar, M. A.; Datla, R.; Sikka, V.; Jones, A.; Choi, C. H. Experimental study of skin friction drag reduction on Superhydrophobic flat plates in high Reynolds number boundary layer flow. *Phys. Fluids.* **2013**, *25*, No. 025103.

(16) Bullee, P. A.; Verschoof, R. A.; Bakhuis, D.; Huisman, S. G.; Sun, C.; Lammertink, R. G. H.; Lohse, D. Bubbly drag reduction using a hydrophobic inner cylinder in Taylor−Couette turbulence. *J. Fluid Mech.* **2020**, *883*, A61.

(17) Peng, C.; Chen, Z.; Tiwari, M. K. All-organic Superhydrophobic coatings with mechanochemical robustness and liquid impalement resistance. *Nat. Mater.* **2018**, *17*, 355−360.

(18) Deng, T.; Varanasi, K. K.; Hsu, M.; Bhate, N.; Keimel, C.; Stein, J.; Blohm, M. Nonwetting of impinging droplets on textured surfaces. *Appl. Phys. Lett.* **2009**, *94*, No. 133109.

(19) Dong, S.; Li, Y.; Tian, N.; Li, B.; Yang, Y.; Li, L.; Zhang, J. Scalable preparation of superamphiphobic coatings with ultralow sliding angles and high liquid impact resistance. *ACS Appl. Mater. Interfaces.* **2018**, *10*, 41878−41882.

(20) Zhang, L.; Xue, X.; Zhang, H.; Huang, Z.; Zhang, Z. Superhydrophobic surface with excellent mechanical robustness, water impact resistance and hydrostatic pressure resistance by two-step spray-coating technique. *Composites Part A: Applied Science and Manufacturing.* **2021**, *146*, No. 106405.

(21) Luo, H.; Yang, M.; Li, D.; Wang, Q.; Zou, W.; Xu, J.; Zhao, N. Transparent super-repellent surfaces with low Haze and high jet impact resistance. *ACS Appl. Mater. Interfaces.* **2021**, *13*, 13813−13821.

(22) Lyu, J.; Wu, B.; Wu, N.; Peng, C.; Yang, J.; Meng, Y.; Xing, S. Green preparation of transparent Superhydrophobic coatings with persistent dynamic impact resistance for outdoor applications. *Chemical Engineering Journal.* **2021**, *404*, No. 126456.

(23) Wang, Y.; Chang, W.; Wang, L.; Zhang, Y.; Zhang, Y.; Wang, M.; Wang, Y.; Li, P. A review of sources, multimedia distribution and health risks of novel fluorinated alternatives. *Ecotoxicology and Environmental Safety.* **2019**, *182*, No. 109402.

(24) Brunet, P.; Lapierre, F.; Thomy, V.; Coffinier, Y.; Boukherroub, R. Extreme resistance of Superhydrophobic surfaces to impalement: reversible electrowetting related to the impacting/bouncing drop test. *Langmuir.* **2008**, *24*, 11203−11208.

(25) Yun, G. T.; Jung, W. B.; Oh, M. S.; Jang, G. M.; Baek, J.; Kim, N. I.; Im, S. G.; Jung, H. T. Springtail-inspired superomniphobic surface with extreme pressure resistance. *Sci. Adv.* **2018**, *4*, No. eaat4978.

(26) Hu, S.; Reddyhoff, T.; Li, J.; Cao, X.; Shi, X.; Peng, Z.; deMello, A. J.; Dini, D. Biomimetic water-repelling surfaces with robustly flexible structures. *ACS Appl. Mater. Interfaces.* **2021**, *13*, 31310−31319.

(27) Hu, S.; Cao, X.; Reddyhoff, T.; Puhan, D.; Vladescu, S. C.; Wang, J.; Shi, X.; Peng, Z.; deMello, A. J.; Dini, D. Liquid repellency enhancement through flexible microstructures. *Sci. Adv.* **2020**, *6*, No. eaba9721.

(28) McCarthy, M.; Gerasopoulos, K.; Enright, R.; Culver, J. N.; Ghodssi, R.; Wang, E. N. Biotemplated hierarchical surfaces and the role of dual length scales on the repellency of impacting droplets. *Appl. Phys. Lett.* **2012**, *100*, No. 263701.

(29) Vasileiou, T.; Gerber, J.; Prautzsch, J.; Schutzius, T. M.; Poulikakos, D. Superhydrophobicity enhancement through substrate flexibility. *Proc. Natl. Acad. Sci. U.S.A.* **2016**, *113*, 13307−13312.

(30) Park, H.; Choi, C. H.; Kim, C. J. Superhydrophobic drag reduction in turbulent flows: a critical review. *Exp. Fluids.* **2021**, *62*, 229.

(31) Lee, C.; Choi, C. H.; Kim, C. J. Superhydrophobic drag reduction in laminar flows: a critical review. *Exp. Fluids.* **2016**, *57*, 176.

(32) Mehanna, Y. A.; Sadler, E.; Upton, R. L.; Kempchinsky, A. G.; Lu, Y.; Crick, C. R. The challenges, achievements and applications of submersible Superhydrophobic materials. *Chem. Soc. Rev.* **2021**, *50*, 6569−6612.

(33) Choi, W.; Kang, M.; Park, J. Y.; Jeong, H. E.; Lee, S. J. Enhanced air stability of Superhydrophobic surfaces with flexible overhangs of re-entrant structures. *Phys. Fluids.* **2021**, *33*, No. 022001.

(34) Lv, C.; Hao, P.; Zhang, X.; He, F. Drop impact upon Superhydrophobic surfaces with regular and hierarchical roughness. *Appl. Phys. Lett.* **2016**, *108*, No. 141602.

(35) Maitra, T.; Tiwari, M. K.; Antonini, C.; Schoch, P.; Jung, S.; Eberle, P.; Poulikakos, D. On the nanoengineering of Super-

hydrophobic and impalement resistant surface textures below the freezing temperature. *Nano Lett.* **2014**, *14*, 172−182.
(36) Tsai, P.; van der Veen, R.; van de Raa, M.; Lohse, D. How micropatterns and air pressure affect splashing on surfaces. *Langmuir.* **2010**, *26*, 16090−16095.
(37) Farooqi, I. S.; Keogh, J. M.; Kamath, S.; Jones, S.; Gibson, W. T.; Trussell, R.; Jebb, S. A.; Lip, G. Y. H.; O'Rahilly, S. Water capture by a desert beetle. *Nature.* **2001**, *414*, 34−35.
(38) Gose, J. W.; Golovin, K.; Boban, M.; Mabry, J. M.; Tuteja, A.; Perlin, M.; Ceccio, S. L. Characterization of Superhydrophobic surfaces for drag reduction in turbulent flow. *J. Fluid Mech.* **2018**, *845*, 560−580.
(39) Bidkar, R. A.; Leblanc, L.; Kulkarni, A. J.; Bahadur, V.; Ceccio, S. L.; Perlin, M. Skin-friction drag reduction in the turbulent regime using random-textured hydrophobic surfaces. *Phys. Fluids.* **2014**, *26*, No. 085108.
(40) Hu, H.; Wen, J.; Bao, L.; Jia, L.; Song, D.; Song, B.; Pan, G.; Scaraggi, M.; Dini, D.; Xue, Q.; Zhou, F. Significant and stable drag reduction with air rings confined by alternated Superhydrophobic and hydrophilic strips. *Sci. Adv.* **2017**, *3*, No. e1603288.
(41) Rong, W.; Zhang, H.; Mao, Z.; Chen, L.; Liu, X. Stable drag reduction of anisotropic Superhydrophobic/hydrophilic surfaces containing bioinspired micro/nanostructured arrays by laser ablation. *Colloids and Surfaces A: Physicochemical and Engineering Aspects.* **2021**, *622*, No. 126712.
(42) Greidanus, A. J.; Delfos, R.; Westerweel, J. Drag reduction by surface treatment in turbulent Taylor-Couette flow. *J. Phys.: Conf. Ser.* **2011**, *318*, No. 082016.
(43) Xu, B.; Li, H.; Liu, X.; Xiang, Y.; Lv, P.; Tan, X.; Zhao, Y.; Sun, C.; Duan, H. Effect of micro-grooves on drag reduction in Taylor−Couette flow. *Physics of Fluids.* **2023**, *35*, No. 043608.